High-Resolution Methane Mapping With the EnMAP Satellite Imaging Spectroscopy Mission

Javier Roger [ID], Itziar Irakulis-Loitxate [ID], Adriana Valverde [ID], Javier Gorroño, Sabine Chabrillat [ID], *Member, IEEE*, Maximilian Brell, and Luis Guanter [ID]

Abstract— Methane (CH_4) mitigation from anthropogenic sources such as in the production and transport of fossil fuels has been found as one of the most promising strategies to curb global warming in the near future. Satellite-based imaging spectrometers have demonstrated to be well-suited to detect and quantify these emissions at high spatial resolution, which allows the attribution of plumes to sources. The PRecursore IperSpettrale della Missione Applicativa (PRISMA) satellite mission (ASI, Italy) has been successfully used for this application, and the recently launched Environmental Mapping and Analysis Program (EnMAP) mission (DLR/GFZ, Potsdam, Germany) presents similar spatial and spectral characteristics (30-m spatial resolution, 30-km swath, about 8-nm spectral sampling at 2300 nm). In this work, we investigate the potential and limitations of EnMAP for CH_4 remote sensing, using PRISMA as a benchmark to deduce its added value. We analyze the spectral and radiometric performance of EnMAP in the 2300-nm region used for CH_4 retrievals acquired using the matched-filter method. Our results show that in arid areas, EnMAP spectral resolution is about 2.7 nm finer and the signal-to-noise ratio values are approximately twice as large, which leads to an improvement in retrieval performance. Several EnMAP examples of plumes from different sources around the world with flux rate values ranging from 1 to 20 t/h are illustrated. We show plumes from sectors such as onshore oil and gas (O&G) and coal mining, but also from more challenging sectors such as landfills and offshore O&G.

We detect two plumes in a close-to-sunglint configuration dataset with unprecedented flux rates of about 1 t/h, which suggests that the detection limit in offshore areas can be considerably lower under favorable conditions.

Index Terms— Environmental Mapping and Analysis Program (EnMAP), matched filter, methane (CH_4), plumes, retrieval.

I. INTRODUCTION

METHANE (CH_4) plays an important role to curb global warming [1]. This is due to its relatively short life in the atmosphere ($\sim$12 years) and because its global warming potential in 20 years is 84 times higher than carbon dioxide (CO_2) [2]. CH_4 anthropogenic emissions mainly originate from agriculture ($\sim$40%), waste management ($\sim$20%), and fossil fuels ($\sim$35%). The latter includes the oil and gas (O&G) industry and coal mining, which have been identified as the most feasible sectors for CH_4 mitigation [3]. A relevant fraction of the emissions from these sectors originate from point sources [4], [5] such as pipeline leaks and venting shafts, which generate more distinct CH_4 plumes than area sources such as landfills.

The higher concentration of CH_4 in plumes from point sources not only categorizes them as significant pollutants and prime targets for mitigation, but also makes them more detectable by spaceborne instruments. It is crucial to identify and monitor these sources as part of a comprehensive CH_4 emission mitigation strategy and imaging spectrometers have proven instrumental in this task [6]. Because of the fine spatial resolution of these instruments, emissions detected in the retrieved CH_4 concentration maps can be attributed to their sources [7]. This attribution leads to the characterization of super emitters and other active sources to guide mitigation [8].

Imaging spectrometers measure radiance at hundreds of spectral bands. Some of them can measure in the visible and near infrared (VNIR: 400–1000 nm) and shortwave infrared (SWIR: 1000–2500 nm), which allows to recreate the radiance spectra along these wavelengths due to the fine spectral sampling and resolution of these instruments. In the SWIR, CH_4 exhibits a weaker absorption window around 1700 nm and a stronger window around 2300 nm. These absorption features can be used to characterize CH_4, which can lead to emission detection.

Currently, there are some operative open-data satellite-based imaging spectrometers such as the Italian PRecursore Iper-

Spettrale della Missione Applicativa (PRISMA) mission [9], the German Environmental Mapping and Analysis Program (EnMAP) mission [10], and NASA'S Earth Surface Mineral Dust Source Investigation (EMIT) mission [11]. EMIT operates differently currently focusing in arid and semiarid regions with no tasking and a spatial resolution and swath of 60 m and 80 km, respectively. On the other hand, both EnMAP and PRISMA operate with tasking, and have a 30 m of spatial resolution and a swath of 30 km, and they present similar spectral resolution and sampling. While PRISMA has already demonstrated its capability to detect CH_4 emissions [6], [12], [13], EnMAP has been recently launched (April 2022) and its capability for CH_4 mapping has not been examined yet. The high similarity of the radiometric and spectral features from both missions and the successful use of PRISMA for CH_4 characterization makes this mission an optimal reference to assess the added value of EnMAP for CH_4 remote sensing. For this reason, we use the comparison to PRISMA as a basis for structuring this study.

In this work, we analyze the spectral and radiometric performance of EnMAP in the 2300-nm window that is going to be used for CH_4 retrievals, using PRISMA as a benchmark. We investigate CH_4 plumes around the world detected with EnMAP datasets in the onshore O&G industry and coal mining areas, but also in more difficult sites to detect CH_4 emissions such as offshore O&G platforms and landfills. Note that we also provide emission quantification estimates although the main focus will be on plume detection using CH_4 concentration mapping.

II. MATERIALS AND METHODS

A. Matched-Filter-Based CH_4 Retrieval Method

CH_4 concentration maps can be retrieved using algorithms based on radiative transfer models [14], [15], or algorithms that mainly exploit the statistics from the image. The latter are low-time consuming and account for radiometric and spectral errors [12]. Thus, we select the matched-filter method [16], [17], which belongs to this group, and that has been extensively used to characterize trace gases in the atmosphere [18], [19]. This algorithm models background radiance as a multivariate Gaussian with mean (μ) and covariance (Σ), assuming a sufficiently homogeneous dataset that exhibits CH_4 enhancement sparsity, i.e., a negligible enhancement that will not affect background characterization. Therefore, pixels containing CH_4 enhancement can a priori be included in the background modelization. Then, shifts from the characterized background radiance are related to CH_4 concentration enhancements [20] according to the following expression:

$$x = \mu + \Delta XCH_4 \cdot t \tag{1}$$

where x is the at-sensor radiance spectrum, t is the target signature that defines the radiance spectrum equivalent to a unit of CH_4 concentration absorption with respect to background, and ΔXCH_4 is the CH_4 concentration enhancement in parts-per-billion (ppb). t results from the product between μ and the unit CH_4 absorption spectrum (k). The latter can be deduced using a lookup table that relates CH_4 transmittance spectra
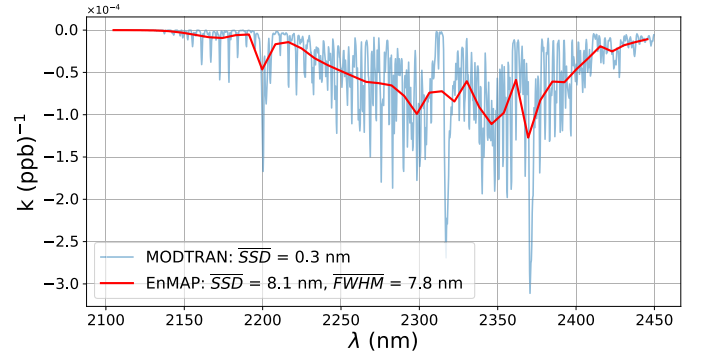

Fig. 1. Unit CH_4 absorption (k) spectra for an EnMAP dataset in the 2300-nm CH_4 absorption window. We difference the MODTRAN-based k spectrum (blue) and the one that results from a subsequent convolution to EnMAP features (red). In the 2300-nm window, the MODTRAN-based mean SSD value is 0.3 nm, while the EnMAP mean nominal values for FWHM and SSD are 7.8 and 8.1 nm, respectively.

obtained using the MODTRAN radiative transfer code [21] to different values of CH_4 column mixing ratio, while accounting for the specific angular configuration at measurement time. For this task, we configure MODTRAN in spectral transmittance mode assuming atmospheric profiles from the U.S. Standard Atmosphere. Then, a fit is applied to relate CH_4 concentration enhancement values to changes in transmisttance spectra, and a subsequent derivative is computed to capture the absorption equivalent to a unit of CH_4 concentration, i.e., the k spectrum. Moreover, the calculation of k for satellite-based instruments also assumes an integration over an 8-km high column [20]. Thus, maximizing the likelihood of the model [22], we can find that ΔXCH_4 can be described as follows:

$$\Delta XCH_4 = \frac{(x - t)^{\mathrm{T}} \Sigma^{-1} t}{t^T \Sigma^{-1} t}. \tag{2}$$

The matched filter applied to the 2300-nm window is a common option in [23], [24], and [25]. We will apply this methodology in the 2100–2450-nm spectral range (see Fig. 1) following the matched-filter implementation shown in [12]. Although the 1700-nm absorption window typically presents higher radiance levels, the absorption is considerably weaker and there are less spectral bands covering this window, which results in noisier CH_4 retrievals.

B. CH_4 Plume Detection and Quantification

Similar to [12], once ΔXCH_4 maps are generated, we search for plumes by visual inspection according to two principles: a CH_4 plume must come from a potential CH_4 emitting source and must follow the wind direction. If we detect a potential plume, we decide whether it is a real plume or a false positive following these principles. First, we check the nature of potential sources by comparison to maps of the spectral radiance from which CH_4 maps are derived and with high-resolution images from Google Earth. Once we verify that it is a potential emitting source, we approximate wind speed to the wind speed at 10 m above the surface (U_{10}) derived from the Global Modelling and Assimilation Office-Forward Processing (GEOS-FP) reanalysis product [26]. If the plume aligns to wind direction, then we can confirm the detection of a plume.

CH$_4$ plume quantification is obtained with the flux rate (Q) parameter, which represents the amount of CH$_4$ being emitted by the source per unit time. It is derived from the plume pixels, which are obtained by the mask that results from applying a plume detection algorithm and a subsequent supervised correction. The algorithm typically takes as an input a mask that results from keeping $>2\sigma$ pixel values. Then, morphology filtering is done in order to discard those clusters not associated with the previously identified plume. Finally, of the remaining clusters, we only keep the cluster referring to the already detected plume.

We express Q in tons per hour (t/h) units, and it is calculated as in [27] with the following expression:

$$Q = \frac{U_{\text{eff}} \cdot \text{IME} \cdot 3.6}{L} \tag{3}$$

where L (m) is the plume size, derived from the square root of the masked area depicting the plume, integrated mass enhancement (IME) is the total excess of CH$_4$ mass (kg) within the plume mask [28], and U_{eff} (m/s) is the effective wind speed. Note that the 3.6 factor converts from kg/s to t/h units. U_{eff} is calculated from the U_{10} data using a linear model based on simulated plumes obtained from large-eddy simulations with the Weather and Research Forecasting Model (WRF-LES) [27], [29] compatible with EnMAP features, and it is expressed as follows:

$$U_{\text{eff}} = 0.34 \cdot U_{10} + 0.44. \tag{4}$$

CH$_4$ plumes observed from space are close to instantaneous observations, which might be the result of highly variable wind speed values through space and time. However, to deduce U_{10}, we use the GEOS-FP reanalysis product, which presents a spatial resolution of $0.25° \times 0.3125°$ and a temporal resolution of 1 h. Thus, we select a U_{10} uncertainty of 2 m/s as in [27], where a study referred to 1-h lasting plumes compared local wind speed values measured at different airports to GEOS-FP values. On the other hand, the IME uncertainty is proportional to the retrieval noise. Then, we calculate the Q uncertainty through the quadratic propagation of the IME and U_{10} uncertainties following (3) and (4). A further assessment regarding quantification is considered out of the scope of this work, as we mainly focus on plume detection using EnMAP data.

C. EnMAP SWIR Spectrometer Characterization in the 2300-nm Window

In this study, we aim to further characterize the radiometric and spectral responses of EnMAP in the 2300-nm window and study their impact on CH$_4$ concentration maps. In the same manner, we will characterize the PRISMA SWIR spectrometer for comparison.

1) Spectral Characterization: At-sensor radiance is transformed into a measurable magnitude following a specific spectral response function (SRF) for each of the spectral bands. The SRF describes the sensitivity of each spectral band to different wavelengths and can be approximated by a Gaussian shape [30], determined by its spectral position (named central wavelength), and the full-width at half-maximum (FWHM). A low value of FWHM will be more sensitive to high-frequency radiance features, but it will receive less radiance because of the narrower spectral range. Central wavelengths and FWHM are parameters that are usually attached to EnMAP datasets. Moreover, low spectral sampling distance (SSD) values across the VNIR and SWIR would lead to a great number of spectral bands that altogether could better define radiance spectra.

The swath of a dataset is captured by a 2-D detector array when measuring with a push-broom imaging spectrometer such as EnMAP. In this kind of instruments, we can find optical aberrations that lead to shifts in central wavelength (also known as spectral smile) and in FWHM [31] in reference to the nominal values. These shifts with respect to the nominal values translate into a deficiency in spectral calibration that disturbs the real values of the SRF parameters. The spectral smile derives from a lack of uniformity across the image, which affects the consistency of data. On the other hand, the spectral resolution is important for CH$_4$ retrieval methods to properly deal with the high-frequency CH$_4$ absorption features [32]. We obtain central wavelength and FWHM shifts as in [12]. We focus the calculation in the 2280–2380-nm spectral range, which is located approximately at the center of the 2300-nm CH$_4$ absorption window.

2) Radiometric Characterization: The signal-to-noise ratio (SNR) reflects the relative proportion between signal and measurement noise. Sufficient high values of SNR would translate into practically insensitive-to-noise results, while lower values of SNR would derive in noisier products. Measurement noise can be expressed by the following expression:

$$\sigma_{\text{MN}} = \sqrt{\sigma_{\text{PS}}^2 + \sigma_{\text{rest}}^2} \tag{5}$$

where σ_{MN} is the total measurement noise, σ_{PS} represents the photon shot noise, and σ_{rest} indicates the noise equivalent to the joint contribution of other noise sources such as the dark current [33]. Photon shot noise comes from the random nature of radiation, which generates a fluctuation in the count of the number of photoelectrons at the detector that can be modeled as a Poisson distribution [34]. Moreover, σ_{PS} is proportional to the square root of radiance, while σ_{rest} is a magnitude independent of radiance. Therefore, given a sufficient high value of radiance, σ_{rest} can become relatively negligible to σ_{PS}. In this case, we can assume that σ_{MN} can be approximated to σ_{PS} and consequently SNR would also be proportional to the square root of radiance. Then, we will calculate SNR in datasets with a high level of radiance in order to scale this magnitude to different radiance values, which would allow us to compare SNR from different datasets.

To calculate the SNR, we first calculate the per-column σ_{MN} spectra following [35]. Note that homogeneous datasets are selected to estimate the SNR because it will facilitate the separation between radiance changes related to surface variability and those coming from measurement noise. Then, the SNR spectra are calculated by dividing the radiance spectra by the resulting σ_{MN} spectra. Assuming an SNR proportionality to the square root of radiance, we can deduce the constant factor array that will allow us to scale SNR to other radiance values. At the same radiance levels, those missions whose

datasets present higher SNR values will have lower σ_{MN}. As a result, there will be a lower impact on the propagation of measurement noise to CH_4 retrievals, which can be deduced by the following expression [36]:

$$\sigma_{\text{RMN}} = \left(t^{\text{T}} \Sigma_{\text{Noise}}^{-1} t\right)^{-1} \quad (6)$$

where σ_{RMN} is the measurement noise contribution to retrieval and Σ_{Noise} is the covariance matrix from the equivalent measurement noise dataset column. Little difference is found between σ_{RMN} values from different columns, and therefore, an averaged spectrum is used as representative of the whole CH_4 retrieval extension.

We also consider the striping, which may result as a consequence of issues such as slight variations in the radiometric response of each across-track detector element and differences in measuring throughout the whole range of across-track pointing [37]. We evaluate this effect in order to assess the viability of applying CH_4 retrieval methodologies to the whole dataset at once or in a per-column basis. One effective method to evaluate striping is to calculate the ratio between adjacent spectral bands from datasets from the same site as done in [38] for EnMAP simulated data. Moreover, we need to isolate striping as the only source of deviation from this value so we will compare datasets from the same site in order to avoid surface variability disturbance. As the spectral smile, a pronounced striping would disturb the consistency between columns. In addition, we also consider polarization as a potential radiometric effect that could introduce additional errors. However, the EnMAP instrument exhibits a low polarization sensitivity ($<5\%$) [10], indicating a minor impact from this effect.

D. EnMAP and PRISMA Data

In this work, we use L1B and L1 level datasets from EnMAP [10] and PRISMA [9] missions, respectively. We compare datasets from both missions to assess whether EnMAP represents an improvement in CH_4 concentration mapping. Datasets with high homogeneity and covering the same area will be the most suitable case for comparison (see Section III-A3). Moreover, to simplify the analysis of the SNR reduction due to degradation, we select an EnMAP dataset acquired close to the end of the Commissioning Phase (CP) (November 1, 2022), when the SNR was measured [39]. Although data tasking was available at the end of 2022, the submitted proposal for tasking was not accepted until mid-December, when the EnMAP instrument unexpectedly turned off. Therefore, the EnMAP dataset used for this comparison was extracted from the archive located at the EnMAP portal [40], where data acquired since April 2022 can be found. Then, we chose an EnMAP dataset from an Agadez Region (Niger) site and a PRISMA dataset in a Sudan site for most comparisons, both in very homogeneous arid areas with similar radiance levels. However, the striping comparison is done with an EnMAP and a PRISMA datasets from the same site in the Ekizak O&G field (Turkmenistan) to discard surface variability as a striping causing factor. Note that we did not select these two datasets for the previous comparison because

TABLE I
INFORMATION ABOUT THE DATASETS USED IN THIS STUDY. DATES ARE IN YYYY-MM-DD FORMAT, AND LATITUDE AND LONGITUDE COORDINATES (LAT/LON) ARE IN DECIMAL DEGREES. DATASETS WITH NO CH_4 EMISSIONS ARE INDICATED WITH $-$ IN THE SECTOR FIELD

Mission	Location	Sector	Date	Lat/Lon
PRISMA	Northern State (Sudan)	$-$	2020-04-01	21.900/ 28.000
PRISMA	Ekizak (Turkmenistan)	Onshore O&G	2022-09-12	38.631/ 54.227
EnMAP	Agadez (Niger)	$-$	2022-07-12	21.328/ 10.477
EnMAP	Khuzestan (Iran)	Onshore O&G	2022-10-22	30.924/ 48.382
EnMAP	Khuzestan (Iran)	Onshore O&G	2022-09-21	31.074/ 48.561
EnMAP	Hassi-Mess. (Argelia)	Onshore O&G	2022-11-17	31.782/ 5.960
EnMAP	Midland B. (U.S.)	Onshore O&G	2022-10-11	32.490/ -102.159
EnMAP	Shanxi (China)	Coal mining	2022-12-05	36.138/ 113.103
EnMAP	Gamyshlja-G. (Turkmenistan)	Onshore O&G	2022-10-02	38.415/ 54.163
EnMAP	Gamyshlja-G. (Turkmenistan)	Onshore O&G	2022-10-06	38.373/ 54.150
EnMAP	Ekizak (Turkmenistan)	Onshore O&G	2022-10-02	38.685/ 54.243
EnMAP	Ekizak (Turkmenistan)	Onshore O&G	2022-10-06	38.643/ 54.233
EnMAP	Gogerendag (Turkmenistan)	Onshore O&G	2022-10-02	38.955/ 54.324
EnMAP	Gogerendag (Turkmenistan)	Onshore O&G	2022-10-06	38.912/ 54.317
EnMAP	Gulf of Mex. (U.S.)	Offshore O&G	2022-07-01	29.029/ -90.370
EnMAP	Delhi (India)	Landfills	2022-11-29	28.554/ 77.209

of the lower homogeneity and the presence of CH_4 emissions. In addition, a comprehensive search for CH_4 plumes was conducted at a wide variety of potential emitting sites. As a result, here, we will illustrate plumes originating in different emission sectors from EnMAP datasets in order to show the detection potential of this mission. We will show datasets from the Ekizak, Gamyshlja Gunorta, and Gogerandag O&G fields in Turkmenistan. Note that CH_4 emissions in some of these fields were already detected in [7]. We will also show datasets from a coal mine site in Shanxi, China, the Hassi Messaoud O&G field in Algeria, a site with a pumping station located in Khuzestan, Iran, the Midland basin part of the Permian Basin (U.S.), an offshore O&G site in the U.S. Gulf of Mexico (GoM), and a Delhi (India) area where the Gazhipur and Okhla landfills are located. Table I reports additional information about every dataset used for this work.

III. RESULTS

A. Performance of the EnMAP SWIR Spectrometer in the 2300-nm Spectral Window

1) Spectral Performance: Fig. 2 shows the across-track variation of channel spectral position and FWHM from arid sites in Sudan (PRISMA) and Niger (EnMAP) in a spectral band representative of the whole 2300-nm absorption window, which are the 2298.42- and 2298.28-nm bands for EnMAP
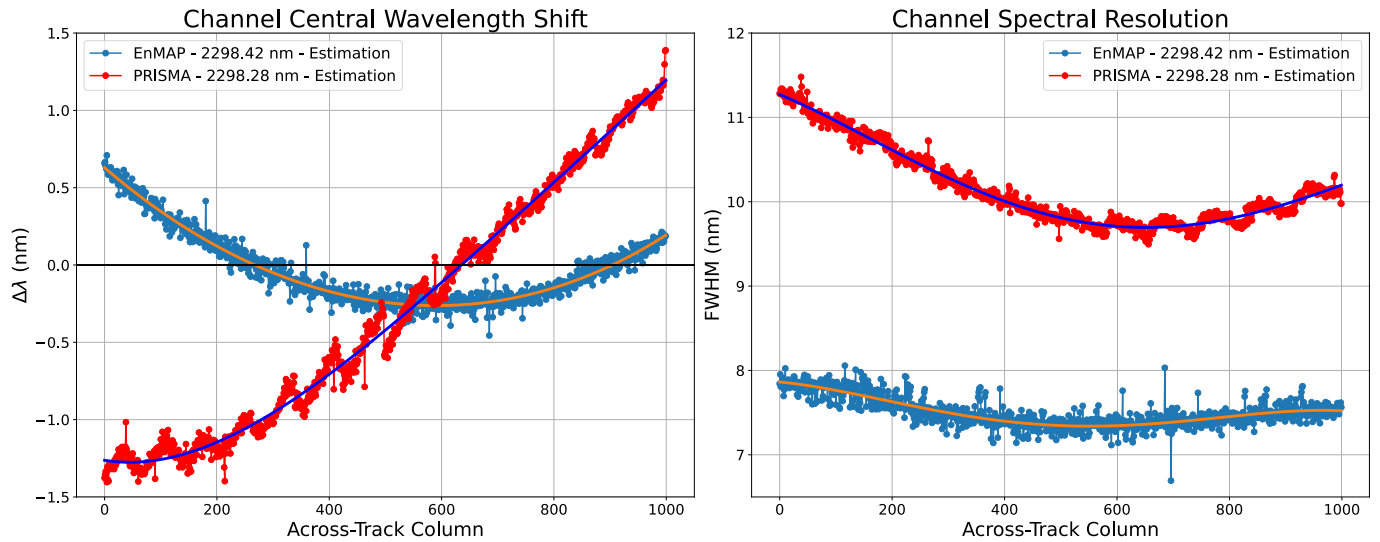
Fig. 2. Spectral smile (left) and spectral resolution (right) spectra in the #143 spectral band (2298.28 nm) from the PRISMA SWIR dataset in a Sudan site and in the #114 spectral band (2298.42 nm) from the EnMAP SWIR dataset in a Niger site.

and PRISMA, respectively. FWHM values accounting for the across-track variations show that on average EnMAP FWHM at ~2300 nm is about 2.7 nm finer than PRISMA FWHM. Therefore, EnMAP can better sample changes in CH$_4$ absorption. A lower FWHM would also imply a lower at-sensor radiance and would lead to a greater measurement noise, but this is compensated because of the greater EnMAP SNR (see Section III-A2). Moreover, the variation from peak-to-peak $\Delta\lambda$ values is lower for EnMAP (1.3 nm) than for PRISMA (2.8 nm). Therefore, EnMAP will be less sensitive than PRISMA to spectral smile, which is translated to a greater uniformity across the image. In addition, the SSD mean values in the 2300-nm absorption window are 8.1 nm for EnMAP and 7.5 nm for PRISMA, which results in a greater number of spectral bands for PRISMA (47 bands) within the 2300-nm window than for EnMAP (43 bands).

2) Radiometric Performance: Fig. 3 shows radiance spectral maps from similar central wavelenghts and equivalent adjacent band ratios from the same Turkmenistan area for EnMAP and PRISMA. The former uses a ratio between the 2104.9-nm band and 2096.0-nm band, while the latter uses one between the 2102.5-nm band and 2094.4-nm band, which are the closest to that of EnMAP. We use spectral bands located at the left shoulder of the 2300-nm absorption window to avoid the interference with CH$_4$ emissions from the scenes. In addition, although there is a temporal difference of 20 days, we can observe that there is little variation in the spatial patterns from one acquisition to the other. We do not show both band ratios using the same color bar range of values because the spectral bands used are slightly different and the datasets are not identical, which results in higher values for the EnMAP band ratio. Therefore, in order to evaluate the general variability, we show both ratios in a range of values comprising their respective mean and standard deviation. We can observe a more pronounced striping pattern in the EnMAP ratio, which would lead to a worse data uniformity for EnMAP than in the PRISMA case. This shows that applying the
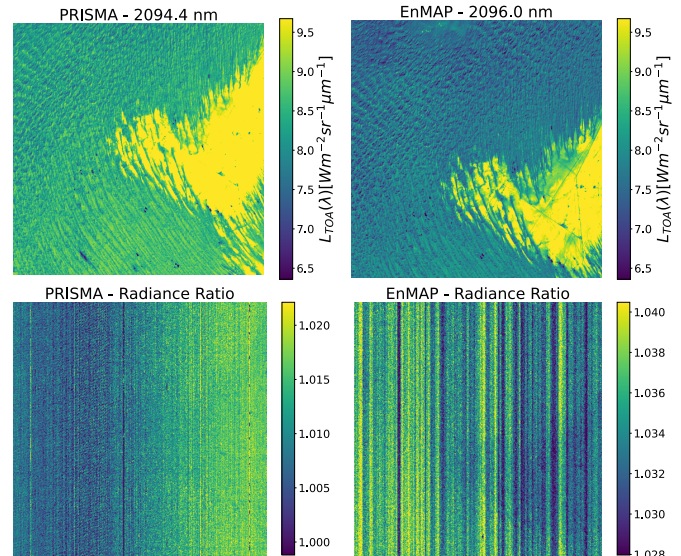

Fig. 3. PRISMA (left) and EnMAP (right) radiance maps at the ~2095-nm spectral bands (top) and ratio between consecutive radiance spectral bands (bottom) over the same O&G area in Turkmenistan.

matched-filter method in a per-column basis is necessary for EnMAP. However, a more progressive pattern due to spectral smile can be observed in the PRISMA case, which confirms the spectral performance results of Section III-A1. Therefore, while EnMAP presents a more remarkable striping, PRISMA shows a higher spectral smile. In the future, further algorithms will be implemented in the EnMAP ground segment to remove striping artifacts [39], so these results are only valid for the EnMAP data from this work.

In Fig. 4, we present the SNR spectra from Niger (EnMAP) and Sudan (PRISMA) datasets and the Niger radiance spectrum in the SWIR. Note that the SNR values from both datasets are comparable because they meet the required conditions (see Section III-A3). Along the SWIR spectral range, EnMAP shows SNR values approximately twice as large as those of
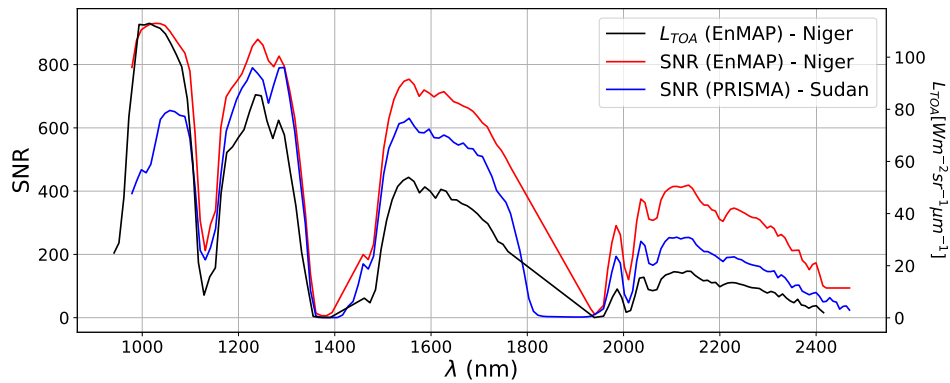
Fig. 4. Top of atmosphere (TOA) radiance (black) and SNR (red) spectra of an EnMAP dataset from a Niger area and an SNR spectrum of a PRISMA dataset from a Sudan area (blue). These parameters are not affected by CH_4 emissions, as no plumes are present in these datasets.

PRISMA in the 2300-nm absorption window. The SNR from the EnMAP SWIR detector array will be reduced from the end of the CP (November 1, 2022) measured values through time due to degradation [39]. Note that the EnMAP dataset was acquired close to this date on July 12, 2022, and therefore, it presents similar SNR values to those at the end of the CP. However, this reduction is not expected to make the SNR lower than the one from the PRISMA SWIR detector array, as the EnMAP one will continue to meet the mission required SNR values for the rest of the instrument's lifetime. This, together with the lower EnMAP FWHM values, will result in a lower retrieval precision error [41]. In addition, we also scaled the EnMAP SNR to the PRISMA radiance (L_{TOA}) following the proportionality with the square root of radiance and we found a negligible difference between the scaled and the unscaled EnMAP SNR spectra that facilitates comparison between datasets.

3) CH_4 Retrieval Performance: We want to characterize and compare CH_4 retrieval random errors from EnMAP and PRISMA missions. To do so, we will calculate the errors related to measurement noise and sensitivity to the background [42] using relatively similar datasets with no CH_4 emissions in order to facilitate the measurement noise deduction. Perfectly homogeneous datasets from the same site with high and equal radiance values would be ideal conditions to compare CH_4 retrievals from both missions. In addition, we also look for EnMAP datasets acquired close to the end of the CP when the SNR values were measured in order to simplify the analysis of the reduction of this parameter due to degradation. However, it is complicated to find datasets that meet these conditions because of the very short operative time of EnMAP and the unexpected instrument turned-off in mid-December. Instead, the Niger and Sudan datasets were used to do this comparison because both present a similar spectral shape along the 2300-nm window and homogeneous arid areas with high and similar radiance levels. This can be seen in Fig. 5 where the spectral slope spectra (top), the averaged radiance (middle), and retrieval CH_4 enhancement distributions (bottom) from both datasets are shown. We can observe a similar spectral slope spectrum from the EnMAP and PRISMA datasets, which indicates a similar surface composition from both sites. On the other hand, the averaged radiance is defined as the mean radiance within the 2300-nm absorption
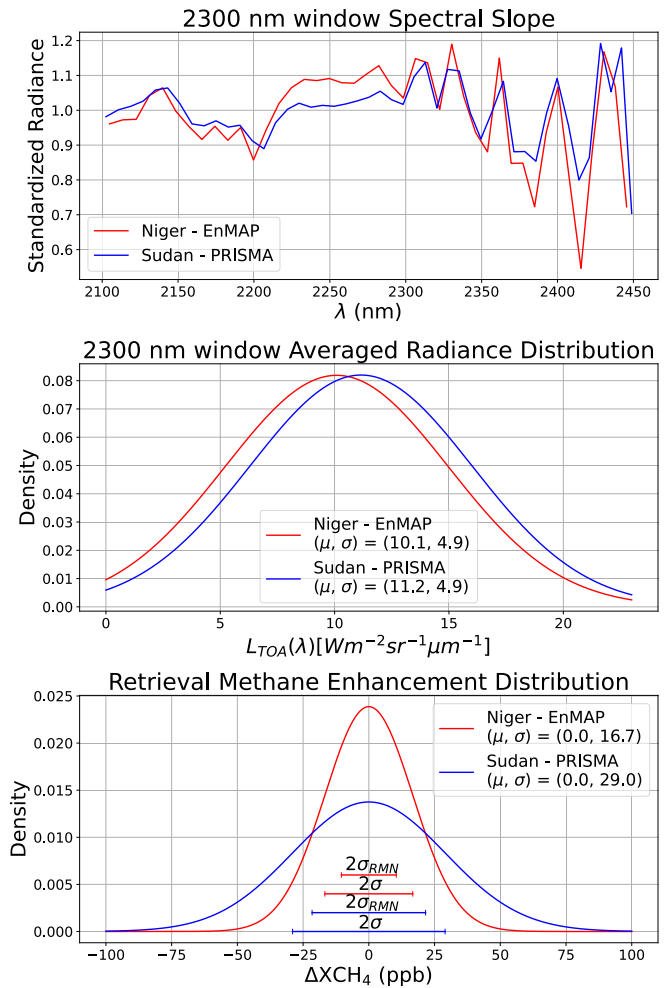

Fig. 5. 2300-nm absorption window spectral slope spectra (top), averaged radiance distribution (center), and retrieval CH_4 enhancement distribution (bottom) from the Niger (EnMAP in red) and Sudan (PRISMA in blue) datasets. μ and σ of the center and bottom panels reflect the mean and standard deviation of their associated Gaussian distributions, while σ_{RMN} reflects the measurement noise contribution to the CH_4 retrieval error.

window and is representative of the radiance level in the matched-filter spectral range of application. Close standard deviation values from averaged radiance histograms confirm a similar surface variability although there is a larger mean value relative difference ($\sim$10%) that questions whether the radiance values are similar enough to be comparable. In order to see the

real impact on retrieval noise, the relative difference between averaged radiance values is propagated first to measurement noise and then to retrieval noise following (5) and (6). We find a negligible disturbance of 1% in the retrieval, which is consistent with the little difference between the not-scaled and scaled SNR EnMAP values from Section III-A2. Therefore, we can assume that CH₄ retrievals from both datasets are comparable. The total retrieval noise can be represented by the CH₄ retrieval standard deviation (σ), derived from the Gaussian distribution followed by the retrieved values. This distribution can be attributed to the central limit theorem, where the combined influence of multiple independent noise sources, such as the measurement noise and the surface variability, converges toward a normal distribution. Then, σ can be reformulated as the square root of the quadratic sum of the measurement noise (σ_{RMN}) and the surface variability noise (σ_{Surf}) contributions ($\sigma = (\sigma_{RMN}^2 + \sigma_{Surf}^2)^{1/2}$). Once we obtain both σ and σ_{RMN}, we can deduce σ_{Surf}. As a result, measurement noise contribution to CH₄ retrieval noise is lower for EnMAP (10.4 ppb) than for PRISMA (21.6 ppb). Moreover, although we have seen a similar surface variability, this contribution is also lower for the EnMAP acquisition (13.1 ppb) than for the PRISMA acquisition (19.4 ppb). Note that, due to the particularly bright and homogeneous areas related to both datasets, we obtain a low retrieval error in comparison to what we would expect in darker and more heterogeneous areas. In addition, we obtain a mean retrieval value (μ) of approximately zero for both datasets although deviations from this value could be found depending on the surface type [12]. Then, we deduce that the lower FWHM from EnMAP can better separate background surface from CH₄ absorption features, whereas the better SSD from PRISMA is not as relevant. This also implies that in more heterogeneous areas, the surface variability contribution to retrieval noise will also be lower in comparison to PRISMA. Thus, this confirms an EnMAP better retrieval performance that would lead to a greater capability to detect CH₄ emissions.

B. Sample EnMAP Plume Detections From Different Source Types

While, in Section III-A, we analyzed the CH₄ retrieval performance from the EnMAP and PRISMA missions, in this section, we will look for CH₄ emissions detected using EnMAP data. Several examples from different parts of the world will be illustrated in order to demonstrate the EnMAP viability for CH₄ mapping.

Previous studies based on spaceborne imaging spectrometers have detected CH₄ plumes coming almost only from coal mining and O&G fields because their point-source nature results in more concentrated plumes that are easier to detect. However, the better retrieval performance of EnMAP has motivated us to search in area sources such as landfills, from where mainly airborne instruments have been able to detect emissions [43]. Additionally, we have also searched on O&G offshore areas, where the typical low radiance values in the SWIR makes plume detection difficult. Offshore CH₄ plumes have been detected from satellite [44] because of
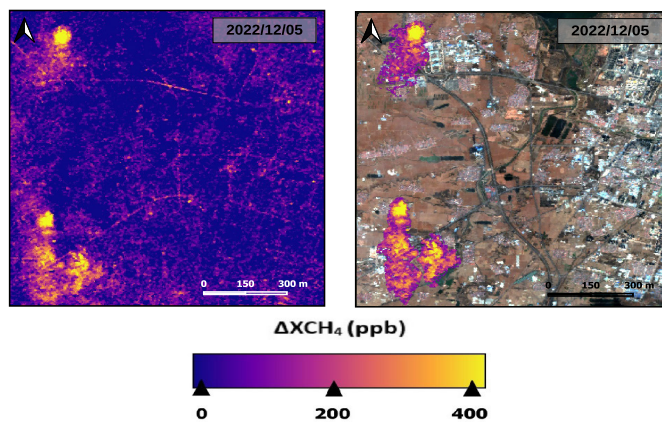

Fig. 6.   CH₄ retrieval (left) and masked plumes (right) of an EnMAP dataset from a coal mining area in the city of Shanxi, on December 5, 2022.

the sunglint effect, which can be better exploited by EnMAP than by PRISMA thanks to its greater across-track pointing range. In addition, we make use of the results from a controlled CH₄ release campaign with satellite overpasses [45], which were conducted over two months and single-blind tests were carried out by six groups that analyzed the data. This campaign validated the ability of EnMAP to estimate flux rates from CH₄ plumes. For this reason, we deduce the flux rate related to each detected emission in this work.

1) Coal Mining in the Shanxi Region (China): In Fig. 6, we show a CH₄ retrieval from an EnMAP dataset in a coal mine region in the city of Shanxi. The low radiance levels and the high heterogeneity of this area generate less robust statistics and therefore results in a poorer performance of the matched filter, i.e., noisier retrievals. This can lead to retrievals where the concentrations from plume pixels are at background noise levels, which difficults the plume detection. This issue can also be observed in other datasets from this study. Additionally, there are surface structures spectrally similar to CH₄ in the 2300-nm absorption window that cannot be separated and therefore are mistaken for CH₄ [18], [46]. This leads to the existence of retrieval artifacts in the CH₄ retrieval that also reduces the potential for plume detection. However, the size and the high concentration of these plumes have allowed their detection. Based on our mapping, we calculated a flux rate of 7.5 ± 4.3 t/h for the plume at the top, and flux rates of $Q = 9.0 \pm 5.1$ t/h and $Q = 6.5 \pm 3.7$ t/h for the two plumes at the bottom at the left and right sides, respectively.

2) Onshore O&G Extraction Facilities in Turkmenistan: We have also been able to detect plumes from point sources from onshore O&G facilities. Some of these emissions were located in an O&G field in Turkmenistan, where we observed CH₄ plumes from the same two sources in two different days (Fig. 7). This shows the ability of satellite-based imaging spectroscopy missions such as EnMAP to monitor persistent CH₄ sources. On the first day (October 2, 2022), the flux rate values were $Q = 21 \pm 5$ t/h and $Q = 18 \pm 4$ t/h from the upper and lower sources, respectively. On the other hand, on the second day (October 6, 2022), the flux rate values were $Q = 13 \pm 4$ t/h and $Q = 14 \pm 5$ t/h from the upper and lower sources, respectively. In addition, the area from this EnMAP
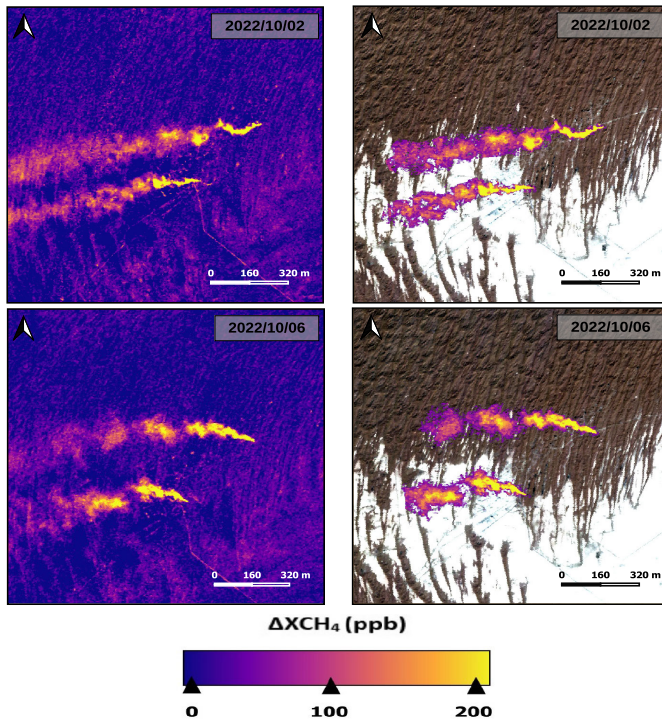
Fig. 7. CH$_4$ retrieval (left) and masked plumes (right) of an EnMAP dataset from an O&G field in Turkmenistan on October 2, 2022 (top) and on October 6, 2022 (bottom).

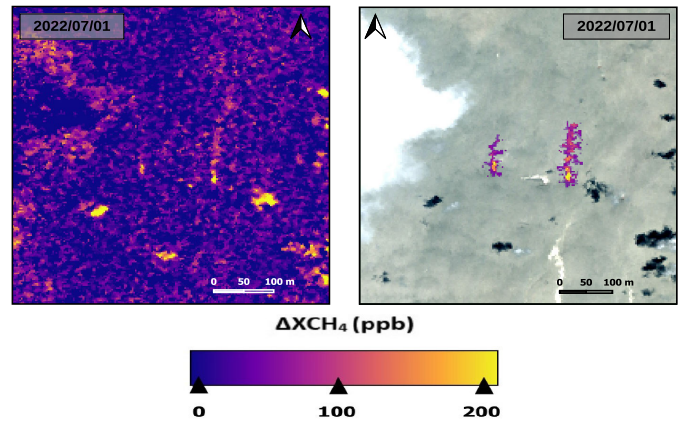

Fig. 8. CH$_4$ retrieval (left) and masked plumes (right) of an EnMAP dataset from an offshore O&G field in the U.S. GoM on July 1, 2022.
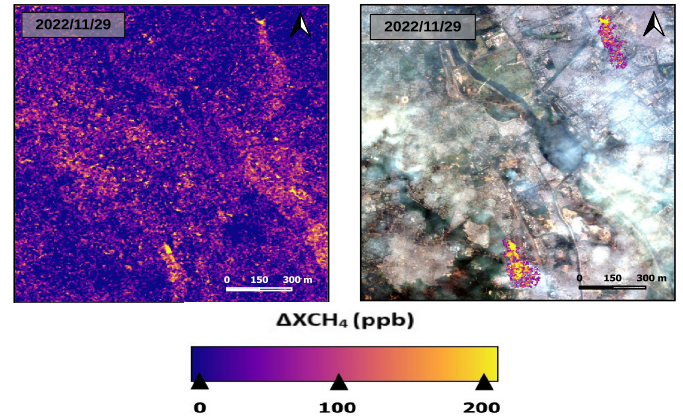

Fig. 9. CH$_4$ retrieval (left) and masked plumes (right) of an EnMAP dataset from a landfill area in Delhi, on November 29, 2022.
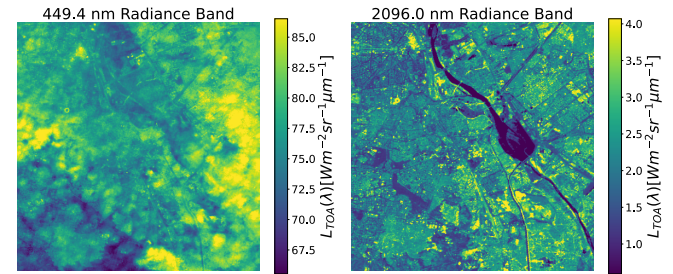

Fig. 10. 449.4- (left) and 2096.0-nm (right) radiance maps of an EnMAP dataset from a landfill area in Delhi. While the 449.4-nm map is covered by disturbing atmospheric elements, surface from the 2096.0-nm map is clearly visible.

dataset is bright and homogeneous, which results in a great performance of CH$_4$ retrieval methods.

3) Offshore O&G Platforms in the U.S. GoM: In general, the high absorption of water in the SWIR spectral range significantly reduces the amount of radiance reaching the sensor unless it is under a specific angular configuration. This will result in noisy CH$_4$ retrievals because very low radiance values will imply measuring out of the sensor dynamic radiance range. However, there is a situation where the CH$_4$ plume detection capability can improve for offshore datasets. This situation is the sunglint effect and it is defined as an increase of water reflectance when the angular configuration between the Sun and the detector approaches a mirror-like configuration. In this configuration, the radiance reaching the detector will be much higher, and therefore, there would be a better chance of detecting CH$_4$ emissions. This is why we look for offshore datasets with angular conditions as close as possible to the mirror-like configuration. The dataset angular configuration is determined by the solar azimuth angle (SAA), the view azimuth angle (VAA), the solar zenith angle (SZA), and the view zenith angle (VZA). In addition, we define the relative zenith angle (RZA), which is expressed as RZA = SZA − VZA, and the relative azimuth angle (RAA), which is expressed as RAA = SAA − VAA. Then, a perfect mirror-like configuration would result in the |RZA|= 0° and |RAA|= 180° values. Across-track pointing from satellite contributes to meet these conditions and therefore a wider pointing range would translate into a higher probability of finding the sunglint effect. EnMAP has a larger available across-track pointing range (±30°) than PRISMA (±21°), which makes EnMAP more suitable to detect offshore CH$_4$ plumes.

Fig. 8 shows two CH$_4$ plumes from offshore O&G platforms in a U.S. GoM site. These platforms are potential emitters since CH$_4$ emissions from this site have been already detected with airborne measurements [47] and also wind speed direction matches the plumes. We find that |RZA| and |RAA| are 23.88° and 19.71°, respectively. These low values generate a close-to-sunglint situation that triggers a high level of radiance, which can be leveraged to detect CH$_4$ plumes. We obtain a flux rate quantification of Q = 0.85 ± 0.38 t/h and Q = 1.2 ± 0.5 t/h for the plume on the left and right sides of the image, respectively. Therefore, this study has shown emissions from offshore O&G platforms with unprecedented low flux rates around 1 t/h. This suggests that in EnMAP,
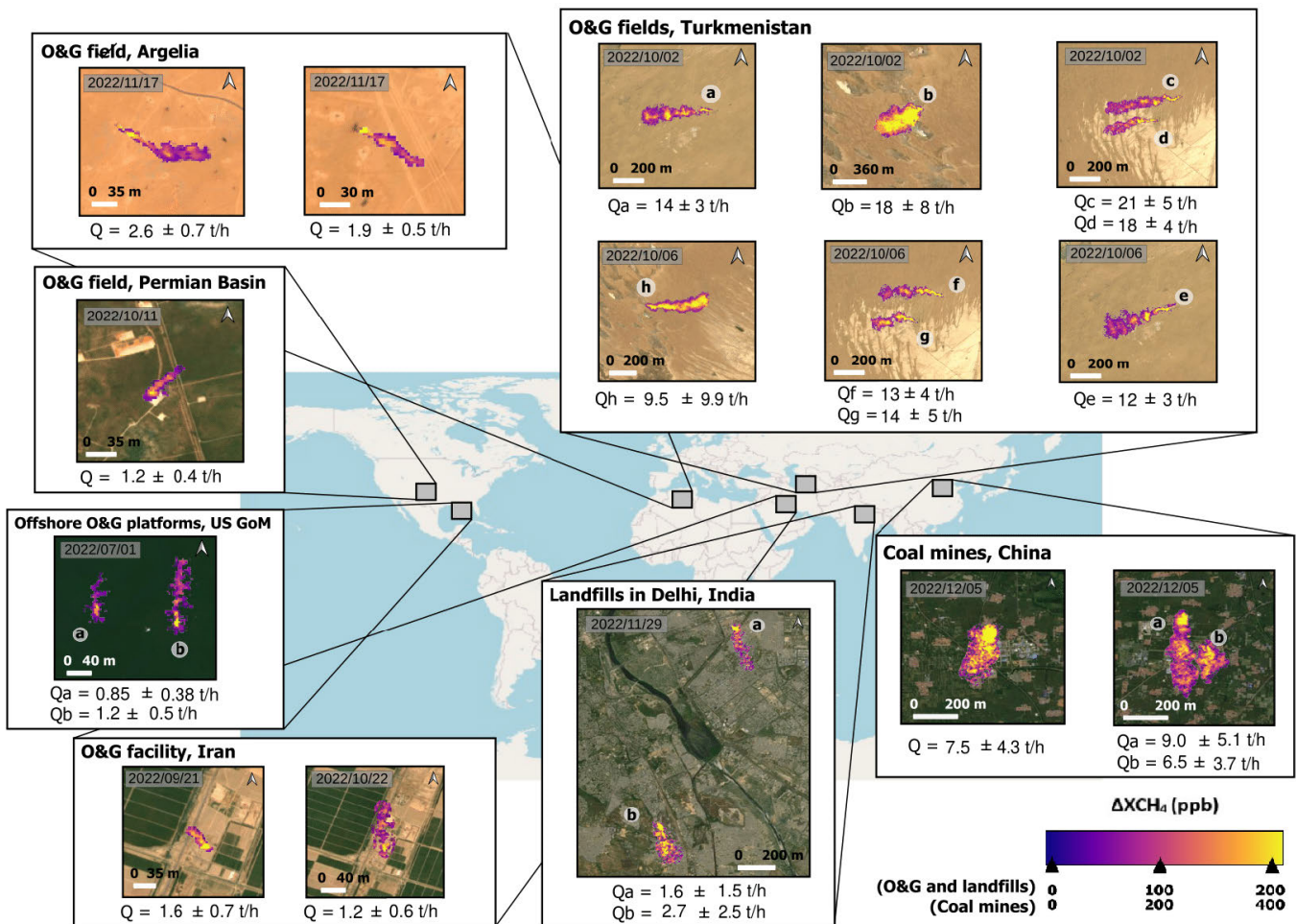
Fig. 11.   Masked CH₄ plumes around the world linked to their flux rate value and overlaid on Google Earth imagery.

the detection limit under favorable conditions can be significantly low to monitor a broad number of offshore platforms.

4) Landfills in Delhi: Point sources have been exploited to detect emissions because they can generate more concentrated plumes that lead to a greater absorption. Meanwhile, CH₄ area sources such as landfills release lower concentrated plumes, which make these emissions difficult to detect. In fact, there are few works done on the satellite observation of CH₄ emissions from landfills [48], [49]. Now, the higher sensitivity to CH₄ from EnMAP could allow the detection of weaker CH₄ plumes from this sector. In Fig. 9, we can see two CH₄ plumes originated from two landfills located in Delhi. We find that plume tails enhancements are almost at background level and the scene presents a high number of retrieval artifacts that disturb the detection of real CH₄ plumes. These emissions are not aligned with the wind speed direction because of the low wind speed value (0.8 m/s) at measurement time, which generates more concentrated plumes that are easier to detect. Moreover, this wind speed low value will generate a relatively high flux rate uncertainty. Additionally, although the scene is covered by disturbing atmospheric elements in the true color image, they can not be seen in the longer wavelengths. These elements gradually disappear as the wavelength increases, and therefore, the SWIR radiance is insensitive

to them. We can observe this in Fig. 10, where we can see that in the 449.4-nm VNIR band, these elements cover most of the scene area, while in a 2096.0-nm SWIR band, this cover does not exist anymore. A possible explanation would be the presence of particles with a size comparable to VNIR and SWIR wavelengths such as in smoke that interact with radiation following the Mie scattering. A high concentration of pollutants of this size is registered in the acquisition date in Delhi [50], where the landfills are located, and therefore, it would explain the lack of visibility across the scene. Thus, since the 2300-nm window is less sensitive to these elements, we have been able to detect these plumes, which establishes the possibility to detect CH₄ area-source emissions from EnMAP datasets. Additionally, flux rate values of $Q = 1.6 \pm 1.5$ t/h and $Q = 2.7 \pm 2.5$ t/h are calculated for the plumes located on the upper and lower parts of the scene, respectively. These calculations are made following an equation calibrated to point-source emissions, which could not be valid for area-source emissions. Nevertheless, due to the large dimension of the plumes, we can approximate these cases to point-source emissions.

5) Plumes Detected Around the World: Along with the examples explored above, in Fig. 11, we illustrate different plumes detected around the world with their corresponding

flux rate values. This shows the EnMAP capability to detect CH_4 plumes in a wide range of different scenarios (variable atmospheric conditions, radiance levels, surface composition, and CH_4 emission flux rates). In addition to the plumes shown in Sections III-B1–III-B4, we find a plume from a Permian Basin (U.S.) site, two other emissions from an O&G field in Algeria, and four more plumes in an O&G field in Turkmenistan. Moreover, we find two plumes from the same pumping station (O&G facility) in Iran, which shows another case of the EnMAP ability to monitor persistent emissions. Additionally, we can see that the flux rates of different plumes range from approximately 1 to 20 t/h. Note that some plumes present a high relative flux rate uncertainty, which is mainly caused by the wind speed. The bigger emissions were originated in the Turkmenistan O&G fields and China coal mines, while the lowest emission was found coming from an offshore O&G platform in the U.S. GoM.

IV. CONCLUSION

In this work, we have studied the spectral and radiometric performance of EnMAP in order to assess their impact on CH_4 retrievals taking PRISMA as a benchmark. In addition, EnMAP plumes coming from different emission sectors are shown to illustrate its ability to map CH_4 emissions.

The spectral and radiometric performance of EnMAP is studied in the 2300-nm absorption window, where the matched-filter method is applied. While PRISMA presents a better SSD and striping, EnMAP presents better FWHM, SNR, and spectral smile. Nonuniformities across the scenes are avoided applying the matched-filter method in a per-column basis. Results indicated that the lower FWHM and higher SNR from EnMAP in the 2300-nm absorption window derive in a lower retrieval noise. Moreover, CH_4 retrievals from datasets around the world demonstrate the capability of EnMAP to detect CH_4 plumes in a wide range of scenarios. In addition to point-source emissions from onshore O&G facilities and coal mines, we have also been able to detect emissions from offshore O&G facilities and landfills. The higher across-track pointing range from EnMAP makes more feasible to find close-to-sunglint measurements where there is a better chance to detect emissions in offshore scenarios and its higher sensitivity to CH_4 makes it more suitable to detect area sources. Definitely, this study shows the important contribution of the EnMAP mission to the current efforts to detect and monitor CH_4 emissions from anthropogenic sources [12].

ACKNOWLEDGMENT

REFERENCES

[1] T. Ming et al., "Perspectives on removal of atmospheric methane," *Adv. Appl. Energy*, vol. 5, Feb. 2022, Art. no. 100085. [Online]. Available: https://www.sciencedirect.com/science/article/pii/S2666792422000038

[2] G. Myhre et al., *Anthropogenic and Natural Radiative Forcing*. Cambridge, U.K.: Cambridge Univ. Press, 2013, pp. 659–740.

[3] UNEP. *Global Methane Assessment: Benefits and Costs of Mitigating Methane Emissions*. [Online]. Available: https://www.unep.org/resources/report/global-methane-assessment-benefits-and-costs- mitigating-methane-emissions, 2021.

[4] M. Omara, D. Zavala-Araiza, D. R. Lyon, B. Hmiel, K. A. Roberts, and S. P. Hamburg, "Methane emissions from U.S. low production oil and natural gas well sites," *Nature Commun.*, vol. 13, no. 1, p. 2085, Apr. 2022, doi: 10.1038/s41467-022-29709-3.

[5] R. Duren et al., "California's methane super-emitters," *Nature*, vol. 575, no. 7781 pp. 180–184, Nov. 2019.

[6] I. Irakulis-Loitxate et al., "Satellite-based survey of extreme methane emissions in the Permian basin," *Sci. Adv.*, vol. 7, no. 27, Jul. 2021, Art. no. eabf4507.

[7] I. Irakulis-Loitxate, L. Guanter, J. D. Maasakkers, D. Zavala-Araiza, and I. Aben, "Satellites detect abatable super-emissions in one of the World's largest methane hotspot regions," *Environ. Sci. Technol.*, vol. 56, no. 4, pp. 2143–2152, Feb. 2022, doi: 10.1021/acs.est.1c04873.

[8] D. Zavala-Araiza et al., "Super-emitters in natural gas infrastructure are caused by abnormal process conditions," *Nature Commun.*, vol. 8, no. 1, p. 14012, Jan. 2017.

[9] R. Loizzo et al., "PRISMA: The Italian hyperspectral mission," in *Proc. IEEE Int. Geosci. Remote Sens. Symp.*, Jul. 2018, pp. 175–178.

[10] L. Guanter et al., "The EnMAP spaceborne imaging spectroscopy mission for Earth observation," *Remote Sens.*, vol. 7, no. 7, pp. 8830–8857, Jul. 2015, doi: 10.3390/rs70708830.

[11] D. S. Connelly et al., "The EMIT mission information yield for mineral dust radiative forcing," *Remote Sens. Environ.*, vol. 258, Jun. 2021, Art. no. 112380. https://www.sciencedirect.com/science/article/pii/S0034425721000985

[12] L. Guanter et al., "Mapping methane point emissions with the PRISMA spaceborne imaging spectrometer," *Remote Sens. Environ.*, vol. 265, Nov. 2021, Art. no. 112671. [Online]. Available: https://www.sciencedirect.com/science/article/pii/S0034425721003916

[13] P. Joyce et al., "Using a deep neural network to detect methane point sources and quantify emissions from PRISMA hyperspectral satellite images," *Atmos. Meas. Techn.*, vol. 16, no. 10, pp. 2627–2640, May 2023.

[14] C. Frankenberg, U. Platt, and T. Wagner, "Iterative maximum a posteriori (IMAP)-DOAS for retrieval of strongly absorbing trace gases: Model studies for CH_4 and CO_2 retrieval from near infrared spectra of sciamachy onboard ENVISAT," *Atmos. Chem. Phys.*, vol. 5, no. 1, pp. 9–22, 2005. [Online]. Available: https://acp.copernicus.org/articles/5/9/2005/

[15] A. K. Thorpe, C. Frankenberg, and D. A. Roberts, "Retrieval techniques for airborne imaging of methane concentrations using high spatial and moderate spectral resolution: Application to AVIRIS," *Atmos. Meas. Techn.*, vol. 7, no. 2, pp. 491–506, Feb. 2014.

[16] D. Manolakis and G. Shaw, "Detection algorithms for hyperspectral imaging applications," *IEEE Signal Process. Mag.*, vol. 19, no. 1, pp. 29–43, Jan. 2002.

[17] D. Manolakis, R. Lockwood, T. Cooley, and J. Jacobson, "Robust matched filters for target detection in hyperspectral imaging data," in *Proc. IEEE Int. Conf. Acoust., Speech Signal Process.-(ICASSP)*, vol. 1, Apr. 2007, pp. I529–I532.

[18] A. K. Thorpe, D. A. Roberts, E. S. Bradley, C. C. Funk, P. E. Dennison, and I. Leifer, "High resolution mapping of methane emissions from marine and terrestrial sources using a cluster-tuned matched filter technique and imaging spectrometry," *Remote Sens. Environ.*, vol. 134, pp. 305–318, Jul. 2013. [Online]. Available: https://www.sciencedirect.com/science/article/pii/S0034425713000977

[19] A. K. Thorpe et al., "Mapping methane concentrations from a controlled release experiment using the next generation airborne visible/infrared imaging spectrometer (AVIRIS-NG)," *Remote Sens. Environ.*, vol. 179, pp. 104–115, Jun. 2016. [Online]. Available: https://www.sciencedirect.com/science/article/pii/S0034425716301250

[20] D. R. Thompson et al., "Space-based remote imaging spectroscopy of the Aliso canyon CH_4 superemitter," *Geophys. Res. Lett.*, vol. 43, no. 12, pp. 6571–6578, Jun. 2016.

[21] (2016). *Spectral Sciencies, Inc.,*. [Online]. Available: http://modtran.spectral.com/

[22] M. Eismann, *Hyperspectral Remote Sensing* (Society of Photo Optical). Bellingham, WA, USA: SPIE Press, 2012, vol. 210.

[23] M. D. Foote et al., "Fast and accurate retrieval of methane concentration from imaging spectrometer data using sparsity prior," *IEEE Trans. Geosci. Remote Sens.*, vol. 58, no. 9, pp. 6480–6492, Sep. 2020.

[24] D. R. Thompson et al., "Real-time remote detection and measurement for airborne imaging spectroscopy: A case study with methane," *Atmos. Meas. Techn.*, vol. 8, no. 10, pp. 4383–4397, Oct. 2015.

[25] P. E. Dennison, A. K. Thorpe, D. A. Roberts, and R. O. Green, "Modeling sensitivity of imaging spectrometer data to carbon dioxide and methane plumes," in *Proc. 5th Workshop Hyperspectral ImageSignal Process. Evol. Remote Sens. (WHISPERS)*, Jun. 2013, pp. 1–4.

[26] A. Molod, L. Takacs, M. Suarez, J. Bacmeister, I.-S. Song, and A. Eichmann. (2012). "The GEOS-5 atmospheric general circulation model: Mean climate and development from MERRA to Fortuna," NASA, Washington, DC, USA, Tech. Rep. TM-2012-104606. [Online]. Available: https://portal.nccs.nasa.gov/datashare/gmao/geos-fp/das/

[27] D. J. Varon et al., "Quantifying methane point sources from fine-scale satellite observations of atmospheric methane plumes," *Atmos. Meas. Techn.*, vol. 11, no. 10, pp. 5673–5686, Oct. 2018.

[28] C. Frankenberg et al., "Airborne methane remote measurements reveal heavy-tail flux distribution in four corners region," *Proc. Nat. Acad. Sci. India A, Phys. Sci.*, vol. 113, no. 35, pp. 9734–9739, Aug. 2016. [Online]. Available: https://www.pnas.org/content/113/35/9734

[29] D. H. Cusworth et al., "Potential of next-generation imaging spectrometers to detect and quantify methane point sources from space," *Atmos. Meas. Techn.*, vol. 12, no. 10, pp. 5655–5668, Oct. 2019.

[30] P. Gege et al., "Calibration facility for airborne imaging spectrometers," *ISPRS J. Photogramm. Remote Sens.*, vol. 64, no. 4, pp. 387–397, Jul. 2009.

[31] L. Guanter, K. Segl, B. Sang, L. Alonso, H. Kaufmann, and J. Moreno, "Scene-based spectral calibration assessment of high spectral resolution imaging spectrometers," *Opt. Exp.*, vol. 17, no. 14, p. 11603, Jul. 2009.

[32] R. O. Green, "Spectral calibration requirement for Earth-looking imaging spectrometers in the solar-reflected spectrum," *Appl. Opt.*, vol. 37, no. 4, p. 683, Feb. 1998.

[33] H. Du, J. Xu, Z. Yin, M. Chai, and D. Sun, "Dark current noise correction method based on dark pixels for LWIR QWIP detection systems," *Appl. Sci.*, vol. 12, no. 24, p. 12967, Dec. 2022. [Online]. Available: https://www.mdpi.com/2076-3417/12/24/12967

[34] B. Luo, L. Yan, and F. Yang, "Research of noise suppression for CMOS image sensor," in *Proc. Int. Conf. Measuring Technol. Mechatronics Autom.*, vol. 2, Mar. 2010, pp. 1100–1103.

[35] D. Thompson et al., (Jul. 2023). *On-Orbit Calibration and Performance of the EMIT Imaging Spectrometer*. [Online]. Available: https://doi.org/10.22541%2Fessoar.168988432.29040205%2Fv1

[36] P. Köhler, L. Guanter, and J. Joiner, "A linear method for the retrieval of sun-induced chlorophyll fluorescence from GOME-2 and SCIAMACHY data," *Atmos. Meas. Techn.*, vol. 8, no. 6, pp. 2589–2608, Jun. 2015.

[37] F. Tsai and W. W. Chen, "Striping noise detection and correction of remote sensing images," *IEEE Trans. Geosci. Remote Sens.*, vol. 46, no. 12, pp. 4122–4131, Dec. 2008.

[38] L. Guanter, K. Segl, and H. Kaufmann, "Simulation of optical remote-sensing scenes with application to the EnMAP hyperspectral mission," *IEEE Trans. Geosci. Remote Sens.*, vol. 47, no. 7, pp. 2340–2351, Jul. 2009.

[39] T. Storch et al., "The EnMAP imaging spectroscopy mission towards operations," *Remote Sens. Environ.*, vol. 294, p. 113632, Aug. 2023. [Online]. Available: https://www.sciencedirect.com/science/article/pii/S0034425723001839

[40] EnMAP. (2022). *Environmental Mapping and Analysis Program (EnMAP)*. [Online]. Available: https: www.enmap.org

[41] D. H. Cusworth et al., "Detecting high-emitting methane sources in oil/gas fields using satellite observations," *Atmos. Chem. Phys.*, vol. 18, no. 23, pp. 16885–16896, Nov. 2018.

[42] D. J. Jacob et al., "Satellite observations of atmospheric methane and their value for quantifying methane emissions," *Atmos. Chem. Phys.*, vol. 16, no. 22, pp. 14371–14396, Nov. 2016.

[43] S. Krautwurst et al., "Methane emissions from a californian landfill, determined from airborne remote sensing and in situ measurements," *Atmos. Meas. Techn.*, vol. 10, no. 9, pp. 3429–3452, Sep. 2017.

[44] I. Irakulis-Loitxate, J. Gorroño, D. Zavala-Araiza, and L. Guanter, "Satellites detect a methane ultra-emission event from an offshore platform in the Gulf of Mexico," *Environ. Sci. Technol. Lett.*, vol. 9, no. 6, pp. 520–525, Jun. 2022, doi: 10.1021/acs.estlett.2c00225.

[45] E. Sherwin et al., "Single-blind test of nine methane-sensing satellite systems from three continents," *EarthArXiv*, 2023, doi: 10.31223/X56089.

[46] A. K. Ayasse et al., "Evaluating the effects of surface properties on methane retrievals using a synthetic airborne visible/infrared imaging spectrometer next generation (AVIRIS-NG) image," *Remote Sens. Environ.*, vol. 215, pp. 386–397, Sep. 2018.

[47] A. K. Ayasse et al., "Methane remote sensing and emission quantification of offshore shallow water oil and gas platforms in the Gulf of Mexico," *Environ. Res. Lett.*, vol. 17, no. 8, Aug. 2022, Art. no. 084039, doi: 10.1088/1748-9326/ac8566.

[48] J. D. Maasakkers et al., "Using satellites to uncover large methane emissions from landfills," *Sci. Adv.*, vol. 8, no. 32, Aug. 2022, Art. no. eabn9683, doi: 10.1126/sciadv.abn9683.

[49] T. Lauvaux et al., "Global assessment of oil and gas methane ultra-emitters," *Science*, vol. 375, no. 6580, pp. 557–561, Feb. 2022, doi: 10.1126/science.abj4351.

[50] PIB Delhi. (2022). *Air Quality Perspective in Delhi*. Accessed: Mar. 1, 2023. Ministry of Environment, Forest and Climate Change. [Online]. Available: https://pib.gov.in/PressReleasePage.aspx?PRID=1888090

Javier Roger received the B.Sc. degree in physics and the M.Sc. degree in remote sensing from the Universitat de Valencia, Valencia, Spain, in 2018 and 2021, respectively. He is currently pursuing the Ph.D. degree in geomatics engineering with the Land and Atmosphere Remote Sensing (LARS) Group, Universitat Politècnica de València (UPV), Valencia.

He is also a member of the LARS Group, UPV. His research focuses on the improvement of methane detection and quantification methods applied to hyperspectral data from missions such as Environmental Mapping and Analysis Program (EnMAP) or PRecursore IperSpettrale della Missione Applicativa (PRISMA). His objective is to provide quality tools to monitor greenhouse gases around the world.

Itziar Irakulis-Loitxate received the B.Sc. degree in geomatic and surveying engineering from the Universidad del Pas Vasco/Euskal Herriko Unibertsitatea, Spain, in 2018, and the M.Sc. degree in remote sensing from the Universitat de Valencia, Valencia, Vitoria-Gasteiz, Spain, in 2019. She is currently pursuing the Ph.D. degree in geomatics engineering with the Land and Atmosphere Remote Sensing (LARS) Group, Universitat Politènica de València (UPV), Valencia.

She is also a member of the LARS Group, UPV. She also works for the International Methane Emission Observatory (IMEO), United Nations Environmental Programme (UNEP), Paris, France. Her research is focused on detecting greenhouse gas emitters, primarily methane emitters, and super pollutants using high-resolution remote sensing data.

Adriana Valverde received the B.Sc. degree in biology from the Universidad de Salamanca, Salamanca, Spain, in 2019, and the M.Sc. degree in geomatics and geoinformation engineering from the Universitat Politècnica de València (UPV), Valencia, Spain, in 2023, where she is currently pursuing the Ph.D. degree in geomatics engineering with the Land and Atmosphere Remote Sensing (LARS) Group.

She is also a member of the LARS Group, UPV. She works on the detection of methane emissions from point source using remote sensing, with the aim of providing global analysis and reporting solutions that can facilitate environmental governance.

Javier Gorroño is currently a Post-Doctoral Scientist with the Universitat Politècnica de València (UPV), Valencia, Spain. He is an expert in the calibration and validation of optical satellite missions. He is currently involved in the development of uncertainty products for the Sentinel 2 mission, the development and validation of methane retrieval algorithms, and the development of satellite intercalibration methodologies.

Dr. Gorroño is a former ESA Living Planet Fellow and also an Active Member of the TRUTHS and Sentinel 2 Next Generation (S2-NG) Mission Advisory Groups.

Maximilian Brell received the Diploma degree in geography from the Dresden University of Technology, Dresden, Germany, in 2011, and the Ph.D. degree from the University of Potsdam, Potsdam, Germany, in 2018.

He currently holds the position of Post-Doctoral Researcher at the Helmholtz Centre Potsdam—GFZ German Research Centre for Geosciences, Potsdam. His area of responsibility is the external validation of the official EnMAP products. His research interests include sensor systems, imaging spectroscopy, LiDAR, CAL/VAL, and sensor fusion.

Sabine Chabrillat (Member, IEEE) received the B.Sc. degree in physics and the Ph.D. degree in imaging spectroscopy from the University of Toulouse, Toulouse, France, in 1990 and 1995, respectively.

After several post-doctoral positions in USA and Germany, she has been holding a tenure senior scientist position at GFZ, Potsdam, Germany, since 2006, where she has been leading a research group on hyperspectral remote sensing applications since 2014. Since 2019, she has been a Science Principal Investigator of the EnMAP German Hyperspectral Satellite. Since August 2021, she has been a Full Professor with the Institute of Soil Science, Leibniz University Hannover, Hannover, Germany, and also holding an associate position at GFZ. Her work focuses on new developments in optical and thermal imaging spectroscopy for soil mapping and monitoring, geoscience, and environmental applications.

Dr. Chabrillat received Lifetime Achievement Award (Marquis Who's Who) in 2017.

Luis Guanter received the B.Sc. degree in physics, and the Ph.D. degree in environmental physics from the Universitat de Valencia, Valencia, Spain, in 2002 and 2007, respectively.

After several post-doctoral positions in Germany and U.K., he became the Head of the Remote Sensing Section, GFZ, Potsdam, Germany, and a Principal Investigator of the Satellite Imaging Spectroscopy EnMAP Mission in 2014. Since March 2019, he has been a Full Professor of applied physics with the Universitat Politècnica de València (UPV), Valencia, where he is leading the Land and Atmosphere Remote Sensing (LARS) Group. Since March 2022, he has been sharing his position at UPV with a methane remote sensing scientist position at the Environmental Defense Fund, Amsterdam, The Netherlands. Now, he is working with the Universitat Politècnica de València.

Dr. Guanter has been included in Clarivate's Highly Cited Researchers List of the world's most influential scientists since 2019.